Formation of fault-related calcite precipitates and their implications for dating fault activity in the East Anatolian and Dead Sea fault zones

P. NURIEL[1]*, G. ROSENBAUM[1], T. I. UYSAL[2], J. ZHAO[3], S. D. GOLDING[1], R. WEINBERGER[4], V. KARABACAK[5] & Y. AVNI[4]

[1]*School of Earth Sciences, The University of Queensland, Brisbane, QLD 4072, Australia*

[2]*Queensland Geothermal Energy Centre of Excellence, The University of Queensland, Brisbane, QLD 4072, Australia*

[3]*Radiogenic Isotope Laboratory, CMM, The University of Queensland, Brisbane, QLD 4072, Australia*

[4]*Geological Survey of Israel, 30 Malkhe Israel Street, Jerusalem 95501, Israel*

[5]*Department of Geology, Eskişehir Osmangazi University, Eskişehir, 26040, Turkey*

**Corresponding author (e-mail: p.nuriel@uq.edu.au)*

Abstract: Fault-related calcite precipitates taken from different segments along the East Anatolian (SE Turkey) and Dead Sea (Israel) fault zones were investigated structurally, geochemically and geochronologically. The results indicate major differences in the nature of calcite precipitates and temporal relationship to faulting. In the Düziçi Fault, calcite-filled veins and hydraulic fractures precipitated co-seismically during three consecutive faulting events. Calcite precipitated in veins at the Har Zefiyya Fault was controlled by near-surface karst processes. Initial opening of the veins occurred prior to about 500 ka and may represent the onset of an east–west contractional deformation. In the Carmel Fault Zone the calcite coating the fault plane precipitated by karst processes, with no evidence of subsequent deformation. Calcite fault gouge from the same site are a mix of host-rock gouge and newly formed authigenic calcite, and their overall geochemistry suggests pervasive fluid–rock interaction in the fault zone. In the Baraq Fault Zone the precipitation of calcite within syntectonic tension gashes and veins occurred prior to 540 ka by the pervasive infiltration of meteoric water into the fault zone. The results demonstrate that geochemical and structural analyses, combined with U–Th geochronology, can shed light on co-seismic and interseismic fault activity, and can potentially provide precise age constraints on the timing of brittle deformation.

Dating fault movements is essential for reconstructing plate tectonic processes and understanding seismic reoccurrence along active faults. Such data can provide valuable information on palaeoseismological activity and verify whether specific structures are likely to be seismically active (e.g. Grant *et al.* 1999). While absolute age dating of minerals from ductile shear zones is becoming a routine (see the review paper by Muller 2003), dating of minerals from brittle fault zones has remained a major challenge. This challenge arises from the incomplete isotopic homogenization of syntectonic minerals due to the low-temperature conditions of their formation.

A large number of studies have focused on the relationship between tectonics and fluid flow, and especially on the geochemistry of fault-related precipitates (e.g. Boles & Grivetti 2000; Labaume *et al.* 2004; Matsuda *et al.* 2004). However, there have been only few attempts to directly constrain the age of fault activity by U–Th geochronology (Szabo & Rosholt 1989; Flotte *et al.* 2001; Verhaert *et al.* 2003, 2004; Uysal *et al.* 2007, 2009, 2011). Carbonate minerals are particularly prone to solution–reprecipitation and/or recrystallization during diagenesis (Folk 1965), which may overprint the primary isotopic signature. This is even more likely to occur within fault zones, where pervasive fluid infiltration is influenced by fracturing. Furthermore, in order to directly relate U–Th ages of calcite precipitates to fault activity, one should demonstrate temporal relationships among faulting, fracturing, fluid circulation and calcite precipitation processes. This challenging task requires a careful utilization of U–Th geochronology combined with geochemical and microstructural studies.

Tension gashes, fault-gouge injection veins, and other syntectonic and co-seismic structures are

From: Fagereng, Å., Toy, V. G. & Rowland, J. V. (eds) *Geology of the Earthquake Source: A Volume in Honour of Rick Sibson*. Geological Society, London, Special Publications, **359**, 229–248.
DOI: 10.1144/SP359.13 0305-8719/11/$15.00

commonly used as indicators for brittle faulting (Boullier *et al.* 2004; De Paola *et al.* 2008). Microstructural studies provide information on the progressive development of veins, temporal changes in conditions of precipitation, and growth mechanisms (Ramsay 1980; Barker *et al.* 2006). In addition, seismological studies have suggested that earthquake-mobilized fluids commonly circulate in fault zones (Secor 1965; Hickman *et al.* 1995; Gratier *et al.* 2002; Miller *et al.* 2004) and such fluids can be responsible for syntectonic mineralization in co-seismic veins and fissures (Sibson 1987; Verhaert *et al.* 2003; Boullier *et al.* 2004), as well as fault-gouge formation (Lin 1996; Vroljik & Van der Pluijm 1999). The geochemistry of fault-related calcite precipitates can therefore provide important information on the fluids that are responsible for their precipitation (Pili *et al.* 2002; Verhaert *et al.* 2004). The type and source of fluids, their transport mechanism and residence time in the system determine the time relationship between faulting, veining and fluid circulation.

This paper combines structural, geochemical and geochronological approaches to investigate fault-related calcite precipitation in the active East Anatolian and Dead Sea fault zones (e.g. Klinger *et al.* 2000; Begin *et al.* 2005). The study areas are respectively in SE Turkey and Israel (Fig. 1a), situated in an intra-continental tectonic setting with major seismic activity documented in historical and archaeological records (i.e. Marco *et al.* 2005; Nemer & Meghraoui 2006). We studied fault-related calcite precipitates in order to determine growth and formation mechanisms, and applied petrographical and cathodoluminescence (CL) approaches to reveal digenetic processes. Using these methods, we can determine whether calcite precipitates have retained their original textures and chemical compositions. We used stable isotope and rare earth element (REE) geochemistry

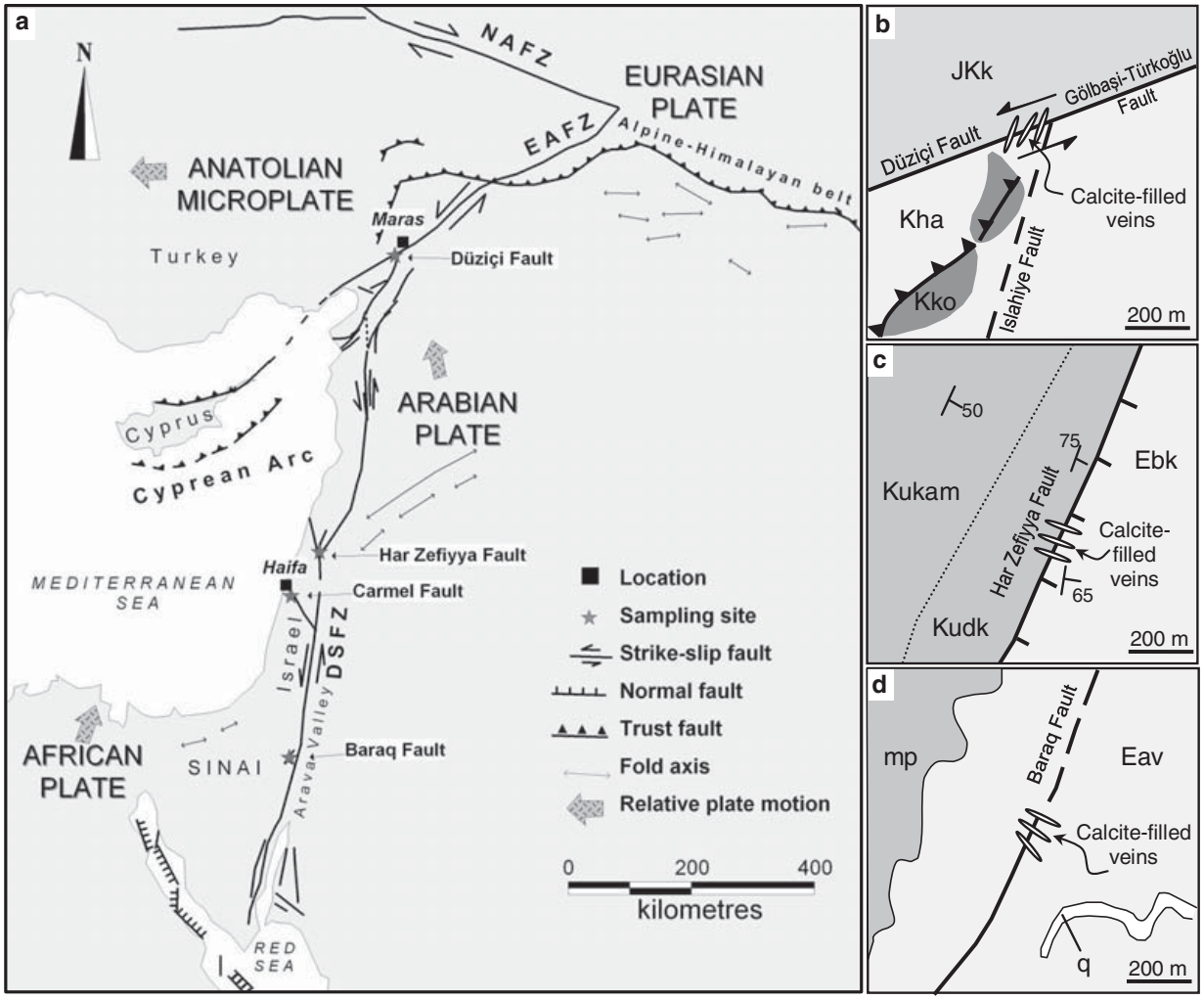

Fig. 1. (**a**) Regional tectonic map of the Eastern Mediterranean (modified after Karabacak *et al.* 2010), showing the locations of the Dead Sea, East Anatolian and North Anatolian fault zones (DSFZ, EAFZ and NAFZ, respectively). The stars mark the four study areas. Schematic maps with faults and veins orientations of (**b**) Düziçi Fault Zone; (**c**) Har-Zefiyya Fault and (**d**) Baraq Fault.

to constrain the origin of fluids and the conditions of precipitation. Here we compare the geochemical signatures of fault-related calcite minerals to those of the country rocks in order to achieve a better understanding of fluid residence time, fluid–rock interactions, and the role and mechanism of fluid mobilization in the fault zone. We performed U–Th dating of calcite minerals of the different types of fault-related precipitates by thermal ionization mass spectrometry (TIMS). We demonstrate and discuss the characteristics of the various types of fault-related calcite precipitates, and the implications of U–Th ages of fault-related precipitates in the context of the local and regional geology of the active strike-slip fault systems.

Geology of the study areas

The study areas are located along an active plate boundary that has evolved since the Miocene owing to a northwards motion of the Arabian and African plates relative to the Eurasia plate (Fig. 1a). The East Anatolian Fault Zone (EAFZ) is a strike-slip fault associated with the westwards escape of the Anatolian block since the mid-Pliocene (Westaway & Arger 1996). The EAFZ is not directly connected to the Dead Sea Fault Zone (DSFZ); the two structures interact in a very complex triple junction near Maraş city in SE Turkey (Fig. 1a). The DSFZ is an approximately north–south-trending strike-slip fault that extends for more than 1000 km, and links the Red Sea divergent plate boundary with the convergent boundary of the Alpine–Himalayan belt in southeastern Turkey (Hempton 1987). It accommodates a sinistral relative plate motion between the Arabian and African plates (Joffe & Garfunkel 1987; Reilinger *et al.* 1997). Activity on the DSFZ commenced in the early–middle Miocene, based on the age of dykes that are offset by the fault zone (Eyal *et al.* 1981; Steinitz & Bartov 1991).

The DSFZ and EAFZ have been the subject of many geophysical and geological studies for several decades (see review papers by Westaway 1994; Garfunkel 1998; Bozkurt 2001; Skobelev *et al.* 2004; Taymaz *et al.* 2004; Mart *et al.* 2005). However, there is only a limited number of direct constraints on the timing of fault activities, most of which are based on palaeoseismological trenching studies involving ^{14}C and optically stimulated luminescence (OSL) dating methods, which are both limited to relatively young events (Amit *et al.* 1999; Marco *et al.* 2005; Zilberman *et al.* 2005; Akyuz *et al.* 2006).

This study focuses on four segments along the EAFZ and DSFZ, which are (from north to south) the Düziçi, the Har Zefiyya, the Carmel and the Baraq faults (Fig. 1a). In the southern part of the EAFZ, the Gölbaşi–Türkoğlu segment has accommodated left-lateral displacement of about 19 km since the Pliocene (4–3 Ma) (Westaway & Arger 1996). The southern continuation of the Gölbaşi–Türkoğlu Fault is the Düziçi Fault segment (Fig. 1b). Recent mapping in this area indicates that the Düziçi Fault is a NE–SW-trending sinistral strike-slip fault that juxtaposes the Upper Jurassic–Lower Cretaceous Karadağ limestone and Upper Triassic–Lower Jurassic Küreci dolomite (JKk in Fig. 1b) against rocks of the Hatay Ophiolites and Koçali Complex (Kha and Kko in Fig. 1b) (Herece 2008). The Düziçi Fault is considered to be an active structure based on deflected young stream beds and faulted Quaternary deposits (Karabacak *et al.* 2010). However, the amount of displacement and the timing of fault activity are unknown.

The Har Zefiyya Fault is a NE–SW-trending fault in the DSFZ in northern Israel (Fig. 1c). The fault shows normal separation between the Bar Kokhba limestone (mid-Eocene; Ebk in Fig. 1c) in the hanging wall and the Deir Hanna Formation (Cenomanian; Kudk in Fig 1c) in the footwall (Sneh & Weinberger 2003). Kinematic indicators suggest a younger reverse motion occurred along this fault (Weinberger *et al.* 2009). There are no age constraints on fault activity; however, calcite separates from fault-plane slickolites have been analysed by U–Th geochronology and found to be older than the age limit of the method, which suggests ages older than 500 ka (Bar-Matthews & Weinberger unpublished data).

The Carmel Fault Zone is a seismically active NW–SE-trending structure that crosses the city of Haifa and is therefore a potential source of seismic hazard (Ben-Menahem & Aboodi 1981; Shapira & Lea 1987; van Eck & Hofstetter 1990). The fault is considered to be a left-lateral strike-slip structure that branches from the DSFZ and transfers part of the left-lateral movement to the Levant continental margin (Rotstein *et al.* 2004; Schattner *et al.* 2006). In the section studied (Fig. 1a), the fault juxtaposes Upper Cenomanian–Turonian limestone (Muhraqa Formation) against Senonian chalk (Menuha Formation), and shows oblique normal and left-lateral sense of movement.

The Baraq Fault (Fig. 1d) is a NE–SW-trending fault that accompanies the western margin of the DSFZ in southern Israel. In the section studied (Fig. 1d), the fault shows normal separation within the Avedat Group (mid-Eocene; Eav in Fig. 1d). The onset of activity on the Baraq Fault is considered to have occurred during the Oligocene (Avni 1997). More recent activity, at 1–2 Ma, is responsible for approximately 100 m of displacement of the Pliocene Arava Formation. Neotectonic activity is known from the incision of rivers

following uplift of about 300–350 m of the Baraq Plateau relative to the Arava Valley (Fig. 1a), and is suggested to have occurred prior to 350 ka (Avni *et al.* 2001).

Methodology

Orientations of fault planes, calcite-filled veins and other calcite precipitates were measured and documented in the field. Various types of fault-related calcite precipitates were collected from four sites (see Table 1), and a detailed petrographical investigation on orientated thin sections was performed with the aim of characterizing calcite crystal morphology and growth history. We used scanning electron microscopy (SEM) and CL microscopy in order to identify deformation and solution–reprecipitation and/or recrystallization diagenesis processes.

Samples were collected from four segments along the EAFZ and DSFZ. In each site, two or three sets of samples were analysed for REE and stable isotopes (Table 1). One set is composed of host-rock samples taken away from the fault zone (HR-8, HR-11 and HR-N2/N3) and is used to compare the composition of undeformed host rock to altered host rock in the fault zone. A second set of samples is composed of host rocks taken directly from vein walls, a few millimetres from calcite-filled vein (marked with HR and associated vein name in Table 1). These samples are used to compare the composition of altered host rock in the deformation zone to calcite-filled vein composition. A third set of samples was taken from calcite-filled veins, fault gouge, and fault planes. The samples were taken from the central part of the veins, excluding samples P7a and P7b that have two sub-samples from different distances from the vein wall. The compositions of this set of samples in comparison with the undeformed and deformed host rock help in determining the fluid composition and water–rock interaction processes.

Oxygen and carbon isotope analyses were carried out in the Stable Isotope Geochemistry Lab at the University of Queensland. The extraction of CO_2 was performed on a CO_2 extraction line for the host-rock samples (see Swart *et al.* 1991 for the procedure used) and using an on-line multi-prep microanalysis system for the calcite precipitates. Isotope measurements were obtained on an Isoprime Dual Inlet stable isotope ratio mass spectrometer (SIRMS) that was calibrated using NBS-18, NBS-19, and ANU-M2 carbonate standards. The $\delta^{13}C$ and $\delta^{18}O$ are compared to V-PDB (Vienna Peedee Belemnite) and V-SMOW (Vienna Standard Mean Ocean Water), respectively, in per mil ‰ and have an analytical reproducibility better than ± 0.1‰ (1σ error).

Rare earth elements were analysed on a Thermo X-series inductively coupled plasma mass spectrometry (ICP-MS) instrument with conditions as described in Lawrence & Kamber (2006). Calcite powders (with dilution factors of *c*. 3000 times, and only a minor ^{43}Ca isotope) were dissolved in a 2% nitric acid solution pre-mixed with internal standards consisting of ^{6}Li, ^{61}Ni, ^{103}Rh, ^{115}In, ^{187}Re, ^{209}Bi and ^{235}U (^{6}Li, ^{61}Ni and ^{235}U are enriched isotopes) for internal correction of mass response drift following the protocol described in Eggins *et al.* (1997). Apart from internal drift correction, the raw data were also corrected for the low, but detectable blank, isobaric interferences from oxides and doubly charged species. The corrected raw data were then externally corrected for additional drift by repeated measurements of a matrix-matched drift-monitoring solution after every five–seven unknown samples being measured. The raw data were converted into concentrations in ppm using two independent digests of the USGS reference material W-2 as the calibration standards. The preferred elemental concentration values of W-2 are those reported in Lawrence & Kamber (2006). In addition, we use JCp-1 coral standard for cross-reference. Our measurements of the JCp-1 standard are in agreement with the values of Inoue *et al.* (2004). The ICP-MS results include measurements of Ca (major element), Mn, Fe and Mg (at ppm level), reported as ratios in Table 1, and yttrium (Y)-REE concentration (at ppm level; Table 2).

U-series dating was carried out in the Radiogenic Isotope Laboratory at the University of Queensland following the analytical procedures described in Zhao *et al.* (2001) and Yu *et al.* (2006). Calcite-powdered samples were completely dissolved in concentrated HNO_3 with a mixed ^{229}Th–^{233}U–^{236}U spike. After digestion, U and Th were co-precipitated with iron hydroxide, and then redissolved in nitric acid prior to purification using conventional anion-exchange column chemistry. The U and Th fractions were then loaded onto zone-refined rhenium filaments, sandwiched in between two graphite layers. Isotope ratios were measured in peak jumping mode on a Daly detector, with Th being measured manually and U automatically on a VG Sector-54 TIMS. The $^{230}Th/^{238}U$ and $^{234}U/^{238}U$ activity ratios were calculated using decay constants of Cheng *et al.* (2000). Non-radiogenic ^{230}Th correction has a minimal impact on the corrected ^{230}Th ages, as the $^{230}Th/^{232}Th$ activity ratios are higher than 100 in most samples. The U–Th ages of all samples from this study are older than 400 ka, at the limit of the U-series dating technique (Ludwig 1991). As calculation of age errors using the usual first-derivative expansion are significantly inaccurate for samples

Table 1. *Stable isotopes, mineralogy and general description of fault-related calcite precipitates*

Sample	$\Delta^{13}C$ ‰ V-PDB	$\delta^{18}O$ ‰ V-SMOW	Mineralogy (XRD)	Mg/Ca	Mn/Fe	Sample type	Structure strike
(1) Düziçi Fault (strike 250°) – *East Anatolian Fault Zone* (SE Turkey)							
J1	−3.9	23.8	Calcite	0.009	0.047	Striated (horisontal) fault plane	250°
J2	−3.4	22.9	Calcite	0.008	0.062	Co-seismic vein	*c.* 210°
J3	−2.9	25.3	Calcite	0.007	0.058	Co-seismic vein	*c.* 200°
J4	−3.0	23.9	Calcite	0.009	0.045	Striated (horisontal) fault plane	*c.* 220°
HR-J2*	0.8	26.3	Calcite	0.072	0.010	Host-rock organic-rich limestone	
(2) Har Zefiyya Fault (strike 010°) – *Dead Sea Fault Zone* (north Israel)							
P7a_0.5–1.0	−11.2	24.3	Calcite	0.002	0.0005	Dilation vein – 0.75 cm from side A	290°
P7a_1.5–3.0	−11.0	24.9	Calcite			Dilation vein – 1.75 cm from side A	290°
P7b_0–0.5	−10.5	24.6	Calcite	0.002	0.0004	Dilation vein – 0.25 cm from side B	295°
P7b_1.5–2.0	−11.0	25.1	Calcite			Dilation vein – 1.75 cm from side B	295°
HR-P7a	−8.8	24.0	Calcite	0.004	0.012	P7a vein-wall host rock	
HR-P7b	−7.6	24.3	Calcite	0.010	0.031	P7b vein-wall host rock	
HR-P8*	−2.9	23.2	Calcite	0.013	0.036	Host-rock limestone (Bar Kokhba Formation)	
(3) Carmel Fault (strike 135°–145°) – *Dead Sea Fault Zone* (north Israel)							
N4	−9.8	26.1	Calcite	0.030	0.0069	Fault-plane coating	144°
N5	−8.6	24.5	Calcite	0.028	0.0006	Fault-plane coating	145°
N6	−10.0	26.2	Calcite	0.013	0.0002	Fault-plane coating	145°
N1	−2.8	30.8	Calcite-dolomite	0.245	0.040	Fault gouge	145°
HR-N2* (HW)	0.5	27.9	Calcite	0.007	0.001	Host-rock chalk (En-Zetim Formation)	
HR-N3* (FW)	1.6	30.1	Dolomite-calcite	0.481	0.012	Host-rock limestone (Muhraqa Formation)	
(4) Baraq Fault (strike 030°) – *Dead Sea Fault Zone* (south Israel)							
R6_2.0–3.0	0.0	29.0	Calcite	0.006	0.008	Fault-plane filling	296°
R8	−0.2	29.0	Calcite	0.004	0.011	Tension gashes	355°
R9_2.5–3.5	0.1	29.1	Calcite	0.005	0.007	Fault-plane filling	305°
HR-R6	0.1	25.1	Calcite	0.017	0.007	R6 vein-wall host rock	
HR-R8	−0.9	25.5	Calcite	0.074	0.009	R8 vein-wall host rock	
HR-R9	−0.2	24.4	Calcite	0.043	0.006	R9 vein-wall host rock	
HR-R11*	0.0	25.7	Calcite	0.026	0.006	Host-rock chalk (Mor Formation)	

* Host-rock samples taken away from the fault zone

Table 2. *Rare earth elements (+Y) concentration (ppm) of fault-related calcite precipitates and their host rocks*

Sample	La	Ce	Pr	Nd	Sm	Eu	Gd	Tb	Dy	Y	Ho	Er	Tm	Yb	Lu
Düziçi Fault															
J1	1.9882	2.7519	0.3954	1.6462	0.4133	0.1200	0.5710	0.0880	0.5132	4.9496	0.1071	0.2517	0.0278	0.1370	0.0171
J2	1.0564	1.5737	0.2291	1.0414	0.2806	0.0833	0.4214	0.0644	0.3943	3.5963	0.0821	0.1934	0.0213	0.1006	0.0122
J3	0.2441	0.2115	0.0256	0.1184	0.0273	0.0104	0.0582	0.0071	0.0446	0.6813	0.0096	0.0206	0.0017	0.0069	0.0006
J4	0.2814	0.3449	0.0488	0.2116	0.0467	0.0140	0.0737	0.0104	0.0590	0.6628	0.0133	0.0312	0.0032	0.0147	0.0020
HR-J2	3.9381	5.5806	0.8533	3.3952	0.6615	0.1598	0.6476	0.0964	0.5463	3.6688	0.1131	0.3178	0.0462	0.2712	0.0401
Har Zefiyya Fault															
P7a_0.5–1.0	0.1078	0.1421	0.0223	0.0817	0.0172	0.0037	0.0189	0.0026	0.0139	0.1084	0.0031	0.0096	0.0012	0.0069	0.0010
P7a_1.5–3.0															
P7b_0–0.5	0.0305	0.0581	0.0070	0.0280	0.0065	0.0014	0.0055	0.0009	0.0045	0.0386	0.0012	0.0032	0.0005	0.0024	0.0004
P7b_1.5–2.0															
HR-P7a	3.7332	6.3911	0.8345	3.2125	0.6422	0.1472	0.6073	0.0906	0.5238	3.5094	0.1115	0.3058	0.0460	0.2792	0.0410
HR-P7b	0.9989	1.7445	0.2109	0.8094	0.1577	0.0352	0.1438	0.0222	0.1321	0.8857	0.0294	0.0829	0.0129	0.0815	0.0122
HR-P8	0.6362	0.9229	0.1210	0.4625	0.0896	0.0221	0.0894	0.0138	0.0832	0.7046	0.0193	0.0545	0.0081	0.0496	0.0082
Carmel Fault															
N4	0.5873	0.6601	0.0912	0.3475	0.0682	0.0169	0.0733	0.0112	0.0727	0.7479	0.0168	0.0513	0.0081	0.0474	0.0078
N5	0.1454	0.2606	0.0213	0.0774	0.0148	0.0040	0.0143	0.0026	0.0156	0.1241	0.0037	0.0104	0.0016	0.0118	0.0018
N6	0.0178	0.0197	0.0028	0.0092	0.0019	0.0005	0.0019	0.0003	0.0017	0.0247	0.0004	0.0013	0.0003	0.0014	0.0002
N1	10.2472	10.2233	1.8517	7.3136	1.4509	0.3645	1.6055	0.2454	1.4683	12.7674	0.3329	0.9590	0.1451	0.8722	0.1321
HR-N2	6.1835	6.1489	1.0836	4.3775	0.8676	0.2223	0.9802	0.1474	0.9017	8.6924	0.2075	0.6163	0.0899	0.5341	0.0837
HR-N3	0.2180	0.3080	0.0373	0.1451	0.0313	0.0076	0.0338	0.0051	0.0297	0.2668	0.0062	0.0183	0.0025	0.0146	0.0022
Baraq Fault															
R6_2.0–3.0	0.1313	0.0524	0.0189	0.0849	0.0168	0.0067	0.0298	0.0047	0.0364	0.7874	0.0111	0.0414	0.0070	0.0448	0.0075
R8	0.0900	0.0290	0.0093	0.0361	0.0060	0.0028	0.0133	0.0025	0.0221	0.4283	0.0070	0.0273	0.0052	0.0374	0.0069
R9_2.5–3.5	0.3266	0.1083	0.0367	0.1392	0.0272	0.0103	0.0434	0.0076	0.0594	0.9776	0.0177	0.0649	0.0114	0.0826	0.0143
HR-R6	8.6647	4.4368	1.4550	6.1717	1.1927	0.3147	1.5955	0.2362	1.5332	14.9180	0.3732	1.1028	0.1656	1.0457	0.1608
HR-R8	13.4150	7.2136	2.1809	9.1167	1.7714	0.4658	2.4028	0.3638	2.4266	26.2840	0.6092	1.8569	0.2895	1.8034	0.2811
HR-R9	4.7660	2.9627	0.8261	3.4256	0.6668	0.1701	0.8588	0.1285	0.8084	7.7429	0.1949	0.5885	0.0923	0.6027	0.0973
HR-R11	6.0440	3.4535	1.0405	4.3813	0.8723	0.2202	1.0746	0.1582	1.0106	9.4518	0.2431	0.7240	0.1132	0.7405	0.1185

with ages of more than 300 ka, we therefore calculated the U/Th age errors by Monte Carlo simulation using Isoplot/Ex Version 2 Program (Ludwig 1991).

Results

Düziçi Fault

Several fault planes with horizontal slickenlines and associated veins are exposed within a small quarry about 20 km south of Maraş city in SE Turkey (Fig. 1a). Faults are subvertical and strike 250° (dipping 72°), with subhorizontal slickenlines pitching 7°E (Fig. 2a). This orientation is in agreement with recent mapping in the area that traced the Düziçi Fault along a NE–SW lineament (Herece 2008). Calcite-filled veins and fissures are distributed throughout the quarry with diverse orientations, and are emplaced in fine-grained, organic-rich limestone host rocks (sample HR-J2 in Table 1). We sampled two calcite-filled veins, which are oriented parallel to fault planes (samples J1 and J4). These veins are up to 100 mm thick and most probably formed by fluid infiltration into the fault zone as evidenced by the presence of slickenline morphology on calcite-filled veins and fault-plane interface (Fig. 2a). The penetrative slickenline morphology indicates that calcite precipitated either in-between faulting events or during faulting. We also sampled two calcite-filled veins from within the fault zone and with no slickenline morphology (sample J2 and J3). Sample J2 is part of a vein that is more than 20 m long and orientated roughly orthogonal to the fault plane. The overall structure of this vein resembles a tension-gash structure (Fig. 2b).

Calcite crystals from the Düziçi Fault are up to 8 mm in size and have a blocky texture. Grains are moderately deformed, and are characterized by twinning and sharp triple-junction grain boundaries (Fig. 3a). Grains do not show growth competition texture or hiatus, and vein filling is somewhat homogenous. Vein-wall host-rock limestone is strongly affected by thin calcite-filled hydraulic fractures with irregular orientation (F in Fig. 3a, b). In all veins, sharp fragments of host-rock material are incorporated into the vein filling and are surrounded by calcite-filled grains (HR in Fig. 3a, b).

X-ray diffraction (XRD) patterns and ICP-MS analyses confirm pure calcite mineralogy for all samples from this site (see Table 1). Petrographical and CL observations indicate high luminescence in both calcite-filled hydraulic fractures and veins (Fig. 3b), implying that both precipitated from similar fluids and with no significant modification by diagenesis. The $\delta^{18}O$ (V-SMOW) and $\delta^{13}C$ (V-PDB) average values of calcite precipitates from this site are 23.9 ± 0.9 and -3.9 ± 0.4‰, respectively (Fig. 4a). A comparison of the $\delta^{18}O$ and $\delta^{13}C$ values of vein-wall host rocks with their calcite precipitates (linked with dashed lines in Fig. 4a) indicates that veins are depleted in both oxygen and carbon isotopes relative to the host rock (up to 3‰ in both; Fig. 4b). The REE patterns of the calcite-filled veins are similar to that of the host-rock sample (HR-J2; Fig. 5a). There is a slight depletion in the HREE composition of the calcite veins in comparison with the host-rock sample and a relatively high REE concentration in the veins in comparison to veins in other sites in this study (Fig. 5b–d). Reliable U–Th ages are obtained for two samples from this site: ages are $405 \pm 15/13$ ka for sample J2; and $501 \pm 44/32$ ka for sample J4-b (a replicate sample J4-a from the same vein was also analysed and yielded a similar age of $525 \pm 50/38$ ka) (see Table 3 and Fig. 6).

Har Zefiyya Fault

An approximately NNE-trending fault plane (dipping 50°) with dip-slip slickenlines, slickenfibres and breccia zone is well exposed. Approximately ESE–WNW-trending calcite-filled veins are distributed within 5 m from the fault plane. Samples P7-a and P7-b were taken from two sides of the same calcite vein (Fig. 2c); the vein is 0.1 m thick and can be traced for 1 m of vertical section. Calcite bands are consistently parallel to vein walls, which are highly brecciated (Fig. 2c). Sample HR-P8 is a relatively unaltered and undeformed limestone host rock of the Eocene Bar-Kokhba Formation, taken about 10 m away from the fault zone. Highly brecciated and altered host-rock samples were taken from both sides of P7 vein walls (HR-P7a and HR-P7b).

Calcite crystals of the Har Zefiyya veins show an elongate-blocky texture. The length to width ratio ranges between 5 and 30, and the maximum grain size is up to 30 mm in length (Fig. 3c). Calcite crystals appear to nucleate from microcrystalline carbonate of wall-rock material (Fig. 3c), and grains are arranged perpendicular to both vein wall and growth laminae (Fig. 3c). Growth competition texture (Kendall *et al.* 1993) is common, especially within the transition from vein wall and following hiatuses in vein growth. The calcite growth direction is inferred from an increase in size and width of crystals in the direction of vein growth (arrows in Fig. 3c). Calcite depositional hiatuses are common, and are characterized by steep-sided and truncated crystal termination. The hiatuses are parallel to growth laminae, and their spacing is between 1 and 10 mm. Fluid or solid inclusion trails, which are common features in veins that are

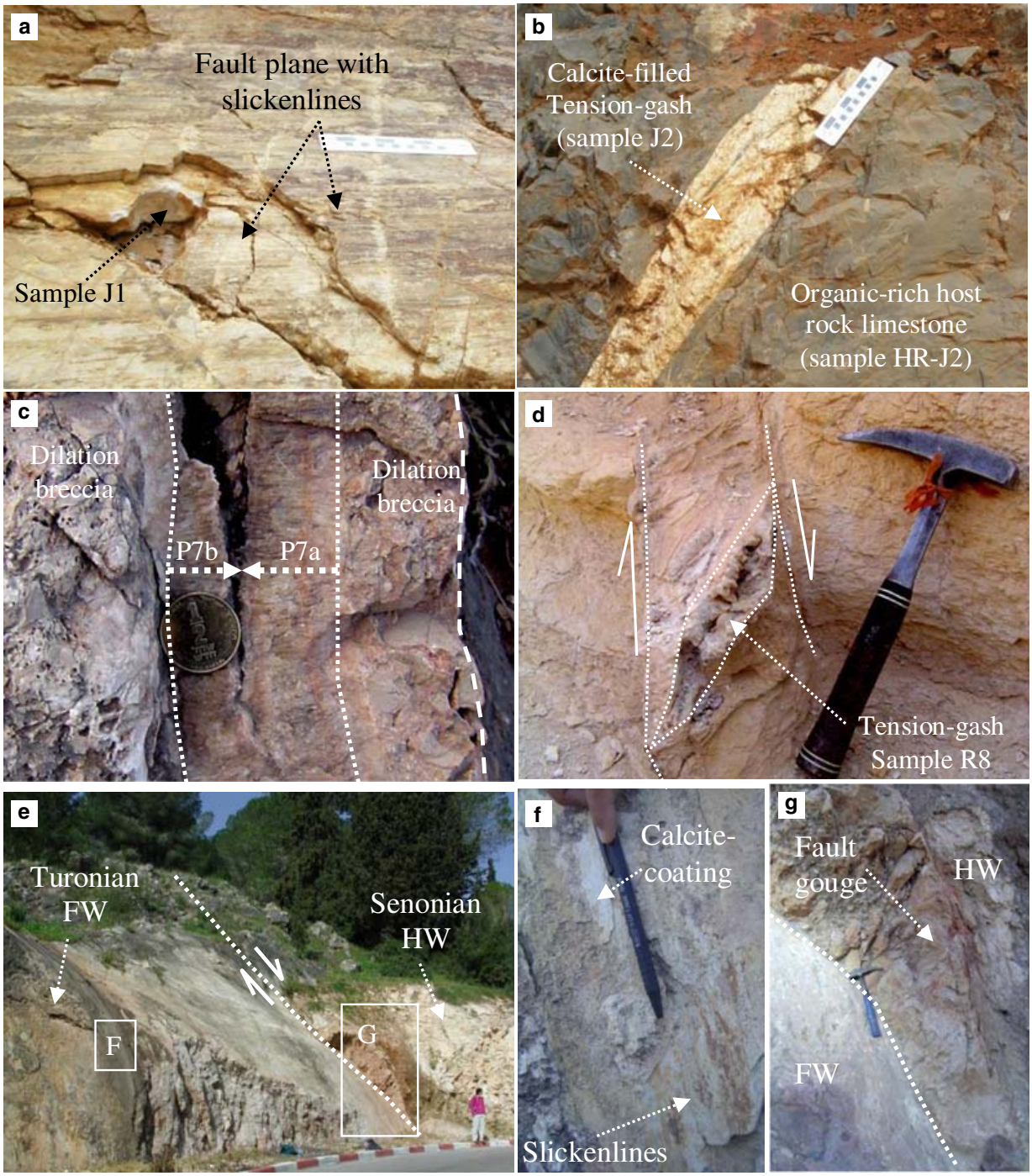

Fig. 2. Fault-related calcite precipitates at the four studied sites. (**a**) Calcite vein within a fault plane with slickenlines morphology taken from the Düziçi Fault Zone. Location of sample J1 is marked (scale bar is 0.2 m). (**b**) Calcite-filled tension-gash vein (sample J2), and host-rock limestone (sample HR-J2). (**c**) Calcite-filled dilation vein in the Har-Zefiyya Fault Zone. (**d**) Calcite-filled tension-gash in the Baraq Fault Zone. (**e**) The Carmel Fault approximately 20 km SE of Haifa city. FW., footwall; HW, hanging wall. (**f**) Calcite-coating fault plane with slickenline morphology taken from the footwall (sample N4; see location in e). (**g**) Reddish-colour calcite fault gouge taken from the fault plane within the hanging wall (sample N1; see location on E).

built-up by successive incremental opening and filling episodes (Ramsay 1980), were not identified.

Vein-filling material was confirmed as pure calcite by XRD analyses (Table 1). Oxygen and carbon isotope ratio values of calcite precipitates in this site are 24.7 ± 0.3 and -11.2 ± 0.2‰, respectively (Fig. 4a). Comparing the $\delta^{18}O$ and $\delta^{13}C$ values of vein-wall host rocks to their calcite precipitates indicates enrichment in oxygen and depletion in carbon isotopes in the veins (2 and

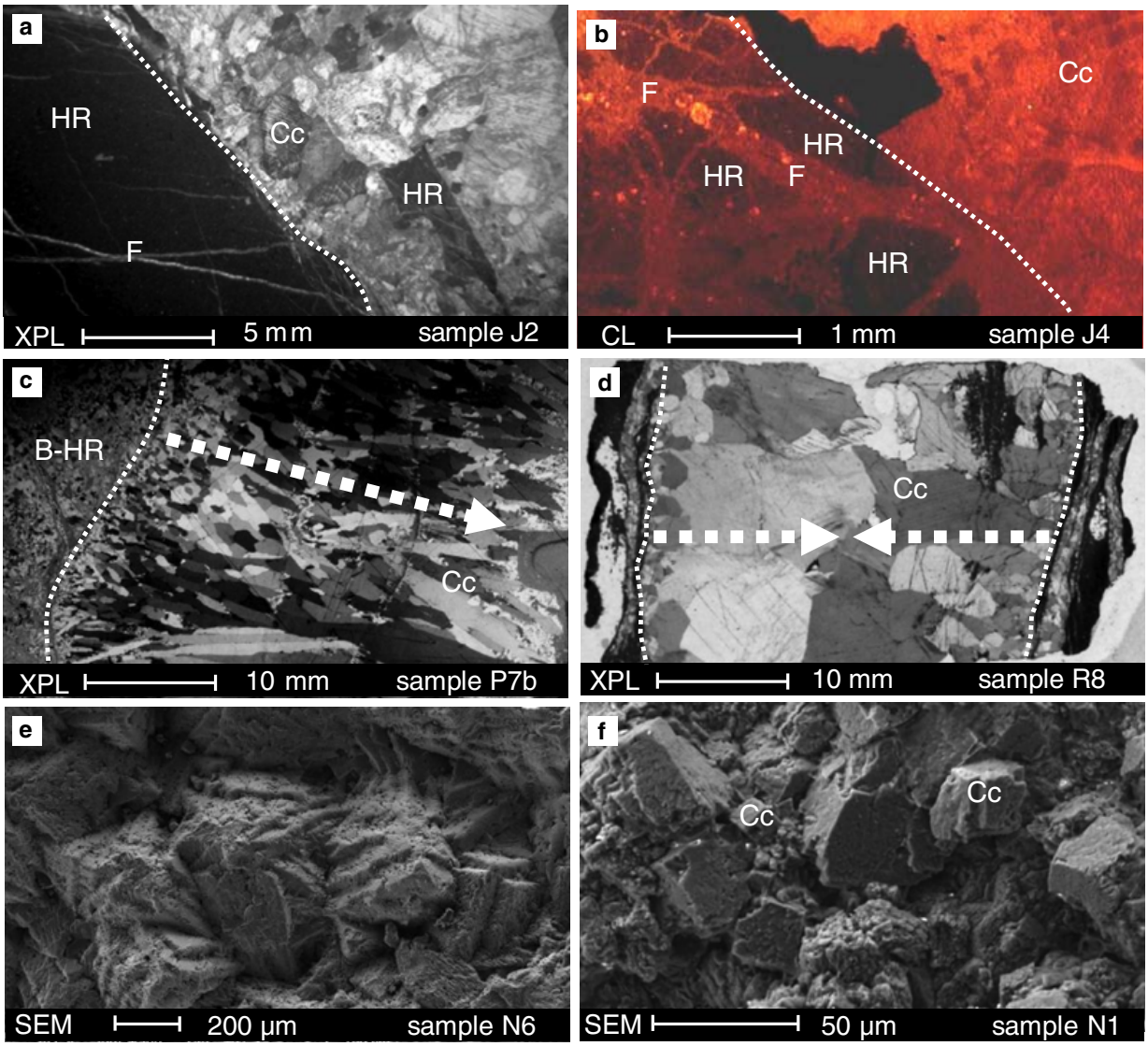

Fig. 3. Microstructures of fault-related calcite precipitates. (**a**) Sample J1 cross-polarized light (XPL). Note the host-rock fragments (HR) within calcite-filling vein (Cc). (**b**) Sample J4 in CL light. Calcite-filled vein (Cc) and fractures (F) showing high luminescence relative to host-rock fragments (HR). (**c**) Sample P7b in XPL. The transition from brecciated host rock (B-HR) to vein filling is marked with a dashed line, and the growth direction is shown with an arrow. (**d**) XPL image of sample R8, showing a growth competition texture from vein walls to vein centre (marked with an arrow). (**e**) SEM image of a calcite-coating fault plane (sample N6). (**f**) Calcite fault gouge (sample N1), showing well-crystallized calcite grains (Ca). SEM conditions: 15 kV, 6 spot size, ×150 and ×1250 magnification (e and f, respectively).

8‰ in oxygen and carbon, respectively; Fig. 4b). The REE pattern of calcite-filled veins is very similar to their host-rock samples, with Ce-negative and Gd- and Y-positive anomalies (Fig. 5b) that are typical of carbonates precipitated in the marine environment (Liu *et al.* 1988, Bolhar *et al.* 2004). The concentration, however, is considerably lower in comparison with the host rocks (Table 2). U–Th ages of subsamples taken close to vein wall in both sides of the vein are at the limit of the U–Th method (P7a_0.5–1 and P7b_0–0.5) and therefore have very large age errors. Two samples taken from the middle part of the vein (P7a_1.5–3 and P7b_1.5–2) gave similar ages of 510 ± 86/58 and 551 ± 110/67 ka, respectively (Fig. 6 and Table 3).

Carmel Fault

A polished and wavy fault plane with slickenlines, breccia and fault gouge (Fig. 2e–g) is exposed about 20 km SE of Haifa city in northern Israel (Fig. 1a). The fault strikes roughly to the SE (dipping 70°), and slickenlines measurements (64°–356°, plunge-trend) indicate oblique normal and sinistral sense of movement. We collected a number of calcite samples taken directly from the

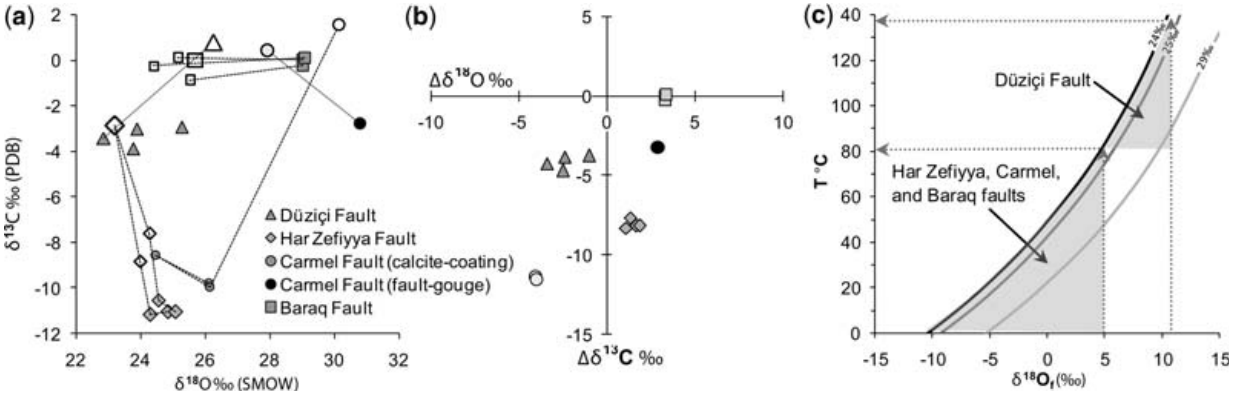

Fig. 4. Stable isotope data. (**a**) Stable isotope values ($\delta^{18}O$ and $\delta^{13}C$) of fault-related calcite precipitates and host-rock samples. The data of the various calcite precipitates samples taken from the four studied sites are shown in filled symbols (see the legend). Analyses of limestone and chalk host-rock samples (see Table 1) taken from each vein wall (linked with dashed line) are also shown (unfilled symbols), together with host-rock values away from fault zone (large unfilled symbols). (**b**) x–y plot of $\Delta\delta^{18}O$ and $\Delta\delta^{13}C$ between vein and host-rock samples away from the fault zone. (**c**) $\delta^{18}O$–temperature plot for calcite-filled veins. The three curves represent the isotopic composition of calcite-filled veins in the Düziçi Fault, Har-Zefiyya and Carmel faults, and the Baraq Fault Zone (24, 25 and 29, respectively) in equilibrium with fluids [$\delta^{18}O_f$ (‰)] from which the calcite precipitated. The curves have been constructed using the calcite–H_2O (liquid) equation of (O'Neil *et al.* 1969). The equilibration temperature was estimated for isotopic composition of H_2O between −15 and 15‰.

fault plane (N4, N5 and N6 in Table 1). These samples are from thin calcite and calcite–dolomite layers that coat the fault plane (Fig. 2f). An SEM image indicates that calcite and dolomite crystals are undeformed and grew under open-space, fluid-fill conditions (Fig. 3e). We also collected a reddish fault gouge, composed of fine-grained calcite (Fig. 2g). An SEM image indicates that this fault gouge is composed of both host-rock crushed material and authigenic calcite minerals (Fig. 3f). For comparison, we sampled a relatively undeformed and unaltered host-rock samples that were taken from the footwall (sample HR-N3) and hanging wall (sample HR-N2).

Calcite-coating fault-plane samples (N4, N5 and N6) and the host-rock sample HR-N2 are pure calcite, based on their XRD pattern and Mg/Ca ratios (Table 1). The host-rock sample HR-N3 and the fault-gouge sample N1 are dolomite–calcite and calcite–dolomite, respectively (Mg/Ca ratio of

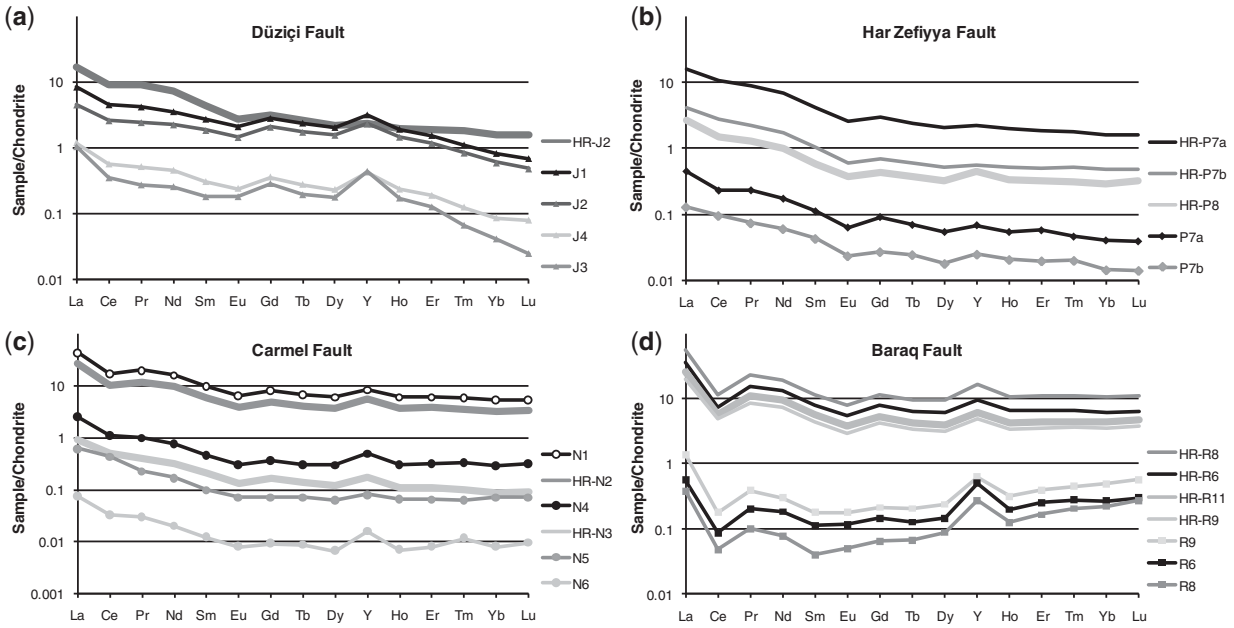

Fig. 5. Chondrite-normalized Y-REE patterns for fault-related calcite precipitates and host-rock samples. The $(Y\text{-}REE)_{CN}$ data are shown for each site: (**a**) Düziçi Fault Zone; (**b**) Har-Zefiyya Fault Zone; (**c**) Carmel Fault Zone; and (**d**) Baraq Fault Zone. Chondrite values from Sun & McDonough (1989).

Table 3. *U–Th age results (ka) of fault-related calcite precipitates*

Sample	U (ppm)	^{232}Th (ppb)	(^{230}Th/^{232}Th)	(^{230}Th/^{238}U)	$\pm 2\sigma$	(^{234}U/^{238}U)	$\pm 2\sigma$	U–Th age (ka)	$+\sigma$	$-\sigma$	Initial ^{234}U/^{238}U	$+\sigma$	$-\sigma$
Düziçi Fault													
J1	0.179	5.07	111	1.0359	0.0057	1.0279	0.0033	>550	290	120	1.170	0.190	0.050
J2	0.095	2.34	133	1.0853	0.0037	1.0819	0.0012	405	15	13	1.260	0.010	0.009
J3	0.135	0.11	3891	1.0225	0.0068	1.0215	0.0014	>550	170	82	1.103	0.054	0.023
J4-a	0.338	7.16	147	1.0293	0.0033	1.0268	0.0012	525	50	38	1.120	0.016	0.011
J4-b	0.224	2.56	269	1.0157	0.0033	1.0185	0.0011	501	44	32	1.077	0.008	0.006
Har Zefiyya Fault													
P7a_0.5–1.0	0.406	15.63	80	1.0129	0.0057	1.0089	0.0019	>550	300	160	1.070	0.086	0.029
P7a_1.5–3.0	0.691	2.62	810	1.0107	0.0056	1.0146	0.0017	510	86	58	1.062	0.014	0.010
P7b_0–0.5	0.443	30.83	43	0.9973	0.0181	1.0092	0.0020	467	210	98	1.036	0.028	0.012
P7b_1.5–2.0	0.785	1.09	2226	1.0146	0.0037	1.0153	0.0025	>550	110	67	1.073	0.020	0.011
Carmel Fault													
N4	0.671	20.82	109	1.1102	0.0061	1.0250	0.0017	–			–		
N5	0.325	3.04	349	1.0779	0.0046	1.0444	0.0021	–			–		
N6	1.478	10.89	458	1.1124	0.0062	1.0596	0.0022	–			–		
Baraq Fault													
R8	0.030	0.18	528	1.0081	0.0095	1.0076	0.0019	>550	260	140	1.046	0.047	0.018
R9_2.5–3.5	0.016	0.82	65	1.0752	0.0056	1.0721	0.0031	417	30	25	1.238	0.016	0.014

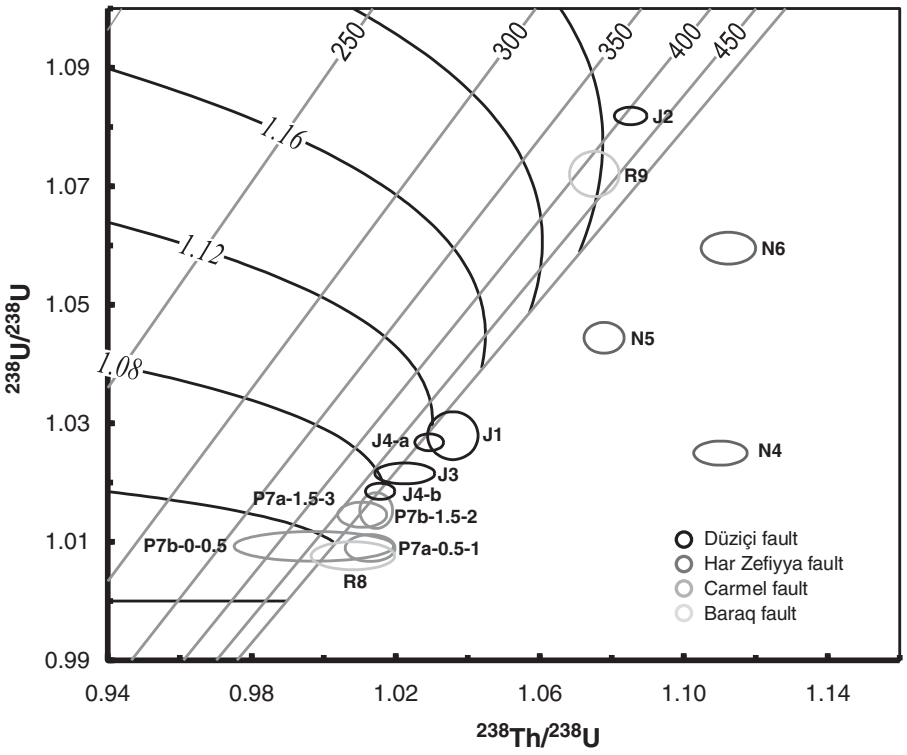

Fig. 6. Plot of activity ratios $^{234}U/^{238}U$ against $^{230}Th/^{234}U$ for fault-related calcite precipitates. Data-point error ellipses are 2σ and are plotted for the Düziçi, Har-Zefiyya, Carmel and Baraq fault zones. The U–Th ages results (in ka) are shown by subvertical grey isochron lines; the evolution curves for $^{234}U/^{238}U$ are in subhorizontal black lines. Note that samples from the Carmel Fault plot outside of the permitted $^{234}U/^{238}U$ evolution curves.

c. 0.5 and 0.25, respectively). Average $\delta^{18}O$ and $\delta^{13}C$ values of calcite precipitates in this site are $25.6 \pm 0.8‰$ and $-9.8 \pm 0.6‰$, respectively. Calcite coating samples are depleted by up to 6 and 10‰ in their $\delta^{18}O$ and $\delta^{13}C$ values relative to their host rocks (Fig. 4b). In contrast, calcite fault gouge is enriched in oxygen and depleted in carbon isotopes (sample N1; up to 3‰ in both). The Y-REE pattern of calcite-coating fault-plane and calcite fault-gouge samples is similar to their host-rock sample (HR-N3 and HR-N2, respectively), with Ce-negative and Y-positive anomalies (Fig. 5c). The concentration in comparison to the host rock is either lower (N5 and N6) or slightly higher (N1 and N4). The $^{230}Th/^{238}U$ and $^{234}U/^{238}U$ activity ratios of calcite-bearing minerals in this site (Fig. 6) deviate from the predicted evolution of ^{238}U decay series during ageing under close-system conditions (Ku 1965). This may suggests open-system conditions with respect to uranium isotopes, meaning that samples may have suffered partial uranium loss due to alteration. U–Th age determination is therefore not possible in this site.

Baraq Fault

Veins and tension gashes in the Baraq Fault Zone have varying orientations (206°–310°) and are filled with gypsum, carbonate, and clay gouge. We sampled a calcite-filled tension-gash vein (sample R8; Fig. 2d), which is associated with two parallel normal faults (dipping 60°). We also sampled two calcite-filled veins orientated parallel to other small-scale normal faults that strike approximately 300° (sample R9 and R6). The veins may have developed either during or after faulting. The host rock is chalk with interbedded chert layers of the lower Eocene Mor Formation. A relatively fresh host-rock sample was taken away from the fault zone for comparison (HR-R11). In addition, rather deformed host-rock samples were separated from vein walls of R6, R8 and R9 (HR-R6 and HR-R8 and HR-R9, respectively).

Calcite crystals are blocky, up to 16 mm long, with a length/width ratio of up to 2 and sharp grain boundaries (Fig. 3d). The transition from vein wall to calcite-vein filling is gradual and hiatuses are prominent close to the vein wall (Fig. 3d). With the exception of sample R9, growth competition textures are somewhat developed (e.g. sample R8; Fig. 3d), allowing the identification of growth direction. Calcite grains appear to nucleate and grow from both sides of the vein wall until the vein closure point at the centre.

All vein-filling material from this site are pure calcite with perfect XRD patterns and Mg/Ca

ratios of less than 0.01 (Table 1). The $\delta^{18}O$ (V-SMOW) and $\delta^{13}C$ (V-PDB) average values of calcite precipitates from this site are 29.0 ± 0.03 and $0.0 \pm 0.15‰$, respectively (Fig. 4a). Stable isotope results indicate that vein-filling calcites are enriched in oxygen (up to 5‰) relative to their host-rock samples, with a very small ($<1‰$) change in carbon isotopes (Fig. 4b). REE concentrations of calcite-filled samples are much lower relative to their host rocks (Table 2). Their pattern, however, is very similar, with Ce-negative and Y-positive anomalies, and a slight enrichment in the HREE composition of calcite precipitates relative to their host rocks (Fig. 5d). U–Th ages were obtained for two samples R8 and R9; however, the age error for sample R8 is too large (Fig. 6). Therefore, only one sample from this site (R9) provided a reliable age of $417 \pm 30/25$ ka (Table 3).

Discussion

The microstructures and geochemistry of fault-related calcite precipitates from the four sites along the EAFZ and DSFZ suggest different formation mechanisms and varying conditions under which calcite precipitated (Fig. 7). We discuss the mechanisms of calcite precipitation and characterize the fluid source, transport, residence time and water–rock interaction. The U–Th ages of all samples from this study are close to the limit of the U-series technique so the age uncertainties are rather high (Fig. 6). However, U/Th ages were still obtained for three of the four sites. We address the implications of U–Th geochronology of the different types of calcite precipitates in terms of their temporal association with fault activity. Finally, we discuss the implications of the U–Th ages in terms of the local and regional geology in four studied segments along the EAFZ and DSFZ.

Calcite precipitates in the Düziçi Fault

Calcite precipitates in the Düziçi Fault Zone are developed either as veins within the fault zone with slickenline morphology (sample J1 and J4) or linked to the fault zone by a calcite-filled hydraulic fracturing system (sample J2 and J3). The lack of internal structures and growth textures, and the presence of angular host-rock fragments within the veins and hydraulic fractures, indicate that precipitation of calcite in these structures was relatively rapid. The similar and rather high luminescence characteristic of calcite-filled veins and fractures, in comparison with the low luminescence of the host rock (Fig. 2b), suggest that both precipitated under similar conditions, from similar fluids, and possibly during the same event. The relative abundance of REE elements (up to 5 ppm; Table 2) and high Mn/Fe ratios (up to 0.06; Table 1) of all calcite-filled veins in this site may account for the observed high luminescence, indicating input of exotic or deep-seated fluids (rich in Mn^{2+} and trace elements) and precipitation under relatively reducing conditions, typical of deep meteoric or burial environments (Janssen *et al.* 2005, 2007).

The Y-REE concentrations in calcite precipitates at this site (Table 2) are much higher than other sites in this study. The fact that calcite precipitate Y-REE patterns preserve the Ce-negative anomaly suggests that fluids inherited their composition from the host rock with some input of exotic fluids. The observed depletion in HREE in the veins relative to the host rock can be explained by the carbonate complexation behaviour of HREE in the host rock. LREE/HREE fractionation can occur as a result of sorption and complexation processes. In the absence of complexing ligands (e.g. carbonate complexes, hydroxide) under acidic condition, fluid REE composition is controlled by sorption, the strength of which increases with decreasing ionic radius from La to Lu, leading to an enrichment of LREE in the fluids

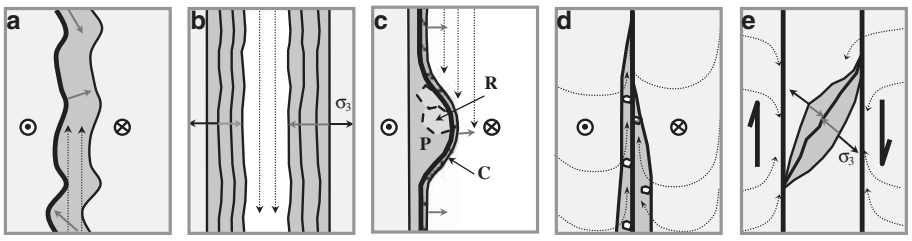

Fig. 7. Types of fault-related calcite precipitates. Calcite precipitation (**a**) in co-seismic veins along fault planes and by upwards-migrating fluids; (**b**) in dilation veins by karst process; (**c**) on fault planes by syntectonic crystallization (R), post-crystallization shear pressure (P) and coating pre-existing slickenlines by karst process (C); (**d**) in fault gouge by pervasive fluid flow; (**e**) in syntectonic tension gash structure and by groundwater infiltration in the fault zone. Fault planes are indicated by thick black lines; fault movement and orientation of tension σ_3 are shown by black arrows. Grey arrows indicate the growth direction of calcite precipitates; black dashed lines indicate fluid circulation in the fault zone.

(Bau & Moller 1992). However, the stability of carbonate complexes of the REE in solution increases from La to Lu, resulting in the dominance of HREE in carbonic fluids. HREE depletion for the calcite veins in the Duzici Fault Zone may indicate that REE mobilization was controlled by sorption processes through the involvement of slightly acidic fluids that circulated deeply into a relatively high-temperature environment (Bau & Moller 1992).

Calcite veins show a conspicuous Y anomaly that provides further information on the fluid-flow event leading to the calcite precipitation. Under most magmatic and sedimentary conditions, Y behaves almost exactly like its geochemical twin Ho. However, under hydrothermal conditions, Y is known to be fractionated from Ho, resulting in suprachondritic Y/Ho ratios >27. For instance, Y/Ho ratios of up to 200 were reported for fluorine-rich medium-temperature hydrothermal fluids (Bau & Dulski 1999), in contrast to typical magmatic and sedimentary values of 24–34. In mildly acidic–mildly basic pH environments and slightly elevated temperatures (>100 °C), fluoride complexes dominate over others (e.g. carbonate, chloride, sulphate, hydroxide) (Wood 1990). The anomalous behaviour of Y is derived from the higher stability of Y over REE complexes over a wide range of temperatures, pH and Eh conditions (Wood 1990). Elevated Y concentrations (Y/Ho up to 70) in the calcite samples can be interpreted as fractionation effects due to complexation during hydrothermal activity. Hydrothermal activity involving (bi)carbonate complexation as mobilizing agent is less likely, because hydrothermal carbonates typically show relative depletion of Y owing to the higher covalent contribution to complexation bonding (Bau & Dulski 1999). Fluoride complexation behaviour changes systematically with temperature. As temperature rises, the stability constants for fluoride (and carbonate) complexes increase for HREE. At the same time, Y also becomes progressively more stabilized as a fluoride complex (Wood 1990); hence, enrichment in Y and HREE is expected to increase with temperature in fluoro-bearing fluids.

Y-REE data in combination with CL examination of vein calcite indicate that fluids derived from deeper reservoirs may have been responsible for carbonate veining in the Duzici Fault Zone. Such deep-seated fluids are likely to have high $\delta^{18}O$ composition relative to meteoric water origin (e.g. Janssen *et al.* 2005). The measured $\delta^{18}O$ (V-SMOW) values of calcite veins in this site are 24‰ (Fig. 4c). Using the calcite–H_2O (liquid) equation of O'Neil *et al.* (1969), and the estimated $\delta^{18}O$ composition of fluids between 5 and 10‰, we can calculate the equilibration temperatures to be between 84 and 133 °C (Fig. 4c).

The calcite-filled hydraulic fractures at this site are similar to co-seismic structures documented in the Nojima Fault Zone in Japan (Boullier *et al.* 2004). Carbonate-filled hydraulic fractures and veins are interpreted to be the result of co-seismic upwards circulation of fluids in the fault zone, and fast nucleation of carbonates attributed to a sudden fluid or CO_2 partial pressure drop due to fracturing (Uysal *et al.* 2009). The above results suggest that calcite in the Düziçi Fault Zone has precipitated co-seismically by a similar mechanism, involving deep-seated fluids migrating upwards in the fault zone during the seismic cycle (Fig. 7a). This notion is supported by the following observations: (1) microstructural evidence for fast growth of calcite-filled veins, incorporated with angular host-rock fragments and precipitation within hydraulic fractures; (2) high Mn/Fe ratio and REE content; and (3) Y-anomaly and $\delta^{18}O$ composition indicative of elevated temperatures (84–133 °C) during precipitation. Thus, U–Th ages seem to provide a good estimation for faulting events, with at least three episodes of faulting indicated by the results. The first generation of vein formation was associated with a calcite-filled fault zone (sample J4). This implies that faulting commenced prior to the precipitation of the calcite in the fault plane. A subsequent faulting event is associated with the co-seismic precipitation of veins in the fault zone. U–Th ages of these specimens (J4a, J4b) are 501–525 ka, implying that the faulting event occurred during that time. A third generation of co-seismic vein formation occurs at 405 ka (sample J2), possibly in association with the formation of post-crystallization fault striae morphology on existing veins.

Calcite precipitates in the Har Zefiyya Fault

Calcite precipitates in the Har Zefiyya Fault Zone are different in their nature and formation mechanism from calcite precipitates in the Düziçi Fault Zone (Fig. 7b). Dilation breccia within vein walls (Fig. 2c) suggests that vein opening was associated with Mode I dilation. The geochemistry of calcite-filled veins indicates near-surface precipitation by karst processes. This view is supported by: (1) significant depletion in carbon isotopes (up to 8‰) with respect to the adjacent host rocks (sample HR-P8; Fig. 4a, b), indicating CO_2-rich fluids, such as meteoric water enriched by C_3-type Mediterranean vegetation (Bar-Matthews *et al.* 1997); (2) stable isotope compositions of calcite dilation veins that are comparable to measured values of oxygen and carbon isotopes in speleothems from the nearby 'Peqi'in cave' (Bar-Matthews *et al.* 2003), suggesting similar conditions of precipitation by

meteoric water at the near-surface and low-temperature environment (Fig. 4c); (3) Y-REE patterns of calcite precipitates (Fig. 5b) which indicate that no major fractionation occurred during precipitation of calcites and that the REE composition of the fluid was mainly controlled by local fluid–rock interaction.

Initiation and opening of Mode I dilation veins may be linked directly to faulting. The east–west orientation of the Har Zefiyya dilation veins reflects a local north–south extension. This deformation is not consistent with normal dip-slip or reactivated reverse movement along the SE-dipping Har Zefiyya Fault (Weinberger *et al.* 2009). However, the formation of such a dilation vein system may represent a stage in deformation that was associated with a regional approximately north–south extension and roughly east–west contraction, as evident in other sites along this sector of the DSFZ (Weinberger *et al.* 2009). Calcite-filling dilation veins have precipitated both a short or a long time after the initial opening, and are most probably controlled by the local hydraulic system. Thus, U–Th ages of calcite precipitate in the veins, especially those obtained close to veins wall, may be regarded as the minimum age for the vein formation. The U–Th age results, although close to the limit of the method, indicate that the initial opening of the vein occurs prior to 550 ka, with continued calcite growth until 510–550 ka. Weinberger *et al.* (2009) suggested that a significant component of east–west regional shortening, normal to the DSFZ, occurred during the late Pleistocene. It is possible that the onset of this deformation stage, prior to 550 ka, is represented by the formation of dilation veins in the Har Zefiyya Fault Zone.

Calcite precipitates in the Carmel Fault

The formation of calcite precipitates on fault plane with slickenline morphology can be attributed to three main mechanisms (Fig. 7c). The first and the most directly associated with faulting is syntectonic crystallization due to pressure solution and reprecipitation processes during faulting. In this case, the U–Th ages correspond to the time of precipitation, which is also the time at which the formation of the slickenlines occurred. The second mechanism is post-crystallization shear pressure (Eyal *et al.* 1992), implying that the formation of slickenlines post-date the formation of the host rock that is affected by them (P in Fig. 7c). The third mechanism is associated with the coating of calcite precipitation along pre-existing grooves within the fault plane (C in Fig. 7c). For the last two mechanisms, U–Th ages only provide minimum age constraints for fault activity.

The distinction between the three mechanisms discussed above can be made based on characteristic microstructures. Syntectonic and post-crystallization formation are characterized by a preferred orientation and/or deformed calcite-grain morphology. In contrast, calcite-coating precipitates simply mimic pre-existing slickenlines morphology and calcite grains are undeformed. SEM images taken both from the top and the bottom views of the calcite layer (less than 5 mm thick) reveal perfect euhedral calcite crystals (Fig. 3e). This observation suggests that calcite samples (N4, N5 and N6) are coating the fault plane, and are precipitated under open-space and fluid-filled conditions. Therefore, these calcite grains were not subjected to subsequent deformation associated with fault slip. The stable isotope composition of calcite coating is very similar to calcite-filled dilation veins in the Har Zefiyya Fault Zone (Fig. 4a), suggesting that calcite precipitated by karst processes, involving CO_2-rich fluids migrating downwards in the fault zone. The U–Th ages of the calcite-coating precipitates may provide a minimum age constraint on the timing of fault activity, as calcite coating post-dated the formation of fault-related slickenlines. However, the U/Th activity ratios of samples from this site (Table 3, Fig. 6) suggest open-system conditions and potential post-formation alteration processes. U–Th age determination is therefore not possible.

Fault gouge is predominantly associated with the mechanical recycling of protolith host rock but can also involve fault-related mineralization (Van der Pluijm *et al.* 2001; Yan *et al.* 2001; Uysal *et al.* 2006). The fault-gouge sample from the Carmel Fault Zone (sample N1) is composed of a calcite and dolomite mixture (Table 1), and the SEM image indicates that a large part of the fault gouge is, in fact, newly grown euhedral calcite grains (Fig. 3f). However, because the two cannot be physically separated, the geochemical results are of a mixed host-rock gouge and authigenic calcite. The similarity of Y-REE patterns of the fault gouge (sample N1, Fig. 3f) and the host rock (sample HR-N2), suggests that the Y-REE composition was dominated by the marine carbonate host rock with the absence of an external fluid. However, unlike the other fault-related precipitates, the calcite fault gouge is enriched in REE relative to the host rock. A range of factors can affect fluid REE characteristics, including pH, release from host minerals and the compositional make-up of the source rock, as well as surface complexation by Fe–Mn oxyhydroxides (Choi *et al.* 2009). Influence of the latter can be seen in the relationship between REE levels in the veins (a proxy to the efficiency of REE scavenging from the fluid into the precipitating carbonate) and the presence of

oxyhydroxide, as approximated by Mn concentrations (108 ppm) and Mn/Fe ratio (0.04; Table 1). Variability in REE concentrations in some veins or fault gouges can be attributed partly to the effect of FeMn-oxyhydroxide scavenging. We proposed that fault gouge in the Carmel Fault Zone is enriched with REE due to pervasive fluid flow and REE scavenged by the calcite fault gouge, as found elsewhere (Pili *et al.* 2002). This is supported by the fact that the Ce-negative and Y-positive anomalies inherited from the sea-water carbonate host rocks is well preserved in the fault gouge sample (Fig. 5c), indicating that fluid was probably equilibrated with the carbonate sequence.

Calcite precipitates in the Baraq Fault

In the Baraq Fault Zone, calcite precipitates are found as tension gashes and veins along fault planes (Fig. 7d). Calcite precipitates are characterized by a growth-competition texture (Fig. 3d), which indicates that vein precipitation occurred over a longer timescale. The REE pattern is similar to the host-rock samples (Fig. 5d), but is two orders of magnitude more depleted, with HREE enrichment in the veins (Table 2). The observed HREE enrichment can be due to complexation processes that are common within shallow groundwater systems (Johannesson *et al.* 1999; Johannesson & Hendry 2000). The rather high $\delta^{18}O$ compositions of calcite-filled veins in this site (29‰; Fig. 4a) are similar to reported values in speleothems from southern Israel (Vaks *et al.* 2010). The increase in $\delta^{18}O$ values in speleothems is considered to reflect the relatively heavy $\delta^{18}O$ composition of rainwater in southern Israel compared with central and northern Israel due to the low amount of precipitation and intense evaporation processes (Vaks *et al.* 2003). Alternatively, the increase in $\delta^{18}O$ values may represent deposition during glacial period (Vaks *et al.* 2010); however, the U–Th age uncertainties are too high to distinguish between glacial and interglacial intervals (sample R9 with $417 \pm 30/25$ ka). In addition, $\delta^{13}C$ values of speleothems usually reflect both the vegetation type and soil–water–rock interaction (e.g. Bar-Matthews *et al.* 1997). At this site, the $\delta^{13}C$ values are relatively high (*c.* 0.02‰; Fig. 4a) and the $\Delta\delta^{13}C$ vein-host rock values are close to zero (Fig. 4b), indicating the very small contribution made by vegetation (mostly C4 type) in this hyper-arid climate of southern Israel (Vaks *et al.* 2010). The results suggest that the fluid source is meteoric water or groundwater (rather than exotic or deep-seated fluid types) with a negligible component of CO_2, and precipitation in the near-surface, low-temperatures environment (Fig. 4c).

The structural observations indicate that tension gashes and fault-parallel fractures are syntectonic fault-driven structures. However, calcite precipitation occurred over a long period of time and during pervasive fluid infiltration into the fault zone. Estimation for calcite growth rate in fissures at near-equilibrium conditions range from 0.12 to 0.22 mm ka^{-1} (Ford *et al.* 1993; Plummer *et al.* 2000). Thus, the U–Th ages can only provide an average age for calcite precipitation in the veins. Considering that an approximately 30 mm-thick calcite vein (sample R9) evolved over a time period of at least 150–250 ka, a calcite average age of $417 \pm 30/25$ ka would suggest a maximum age for calcite precipitation of around 540 ka. Age constraint on the youngest activity along the Baraq Fault is considered to be prior to 350 ka. This age is based on estimation of the timing of erosion following major tectonic movement along the fault (Avni *et al.* 2000). It is possible that the formation of the syntectonic vein structures is associated with the youngest activity along the Baraq Fault.

Conclusions

The microstructures and geochemistry of fault-related calcite precipitates indicate different conditions under which calcite precipitate in fault zones. Our conclusions from the four studied sites are as follows.

- In the Düziçi Fault Zone, calcite-filled veins and hydraulic fractures precipitated co-seismically from deep-seated fluids that migrated upwards into the fault zone during the seismic cycle. The precipitation was associated with the fast nucleation of carbonates attributed to a sudden fluid or CO_2 partial pressure drop caused by fracturing. The U–Th ages in this site indicate at least three consecutive faulting events: prior to 525 ka; during 525–501 ka: and at approximately 405 ka.
- In the Har Zefiyya Fault Zone, the geochemistry of calcite-filled dilation veins indicates that precipitation of calcite occurred by karst processes in the near-surface environment. The U–Th ages indicate that initial opening of the vein occurred prior to about 550 ka. This age is temporally associated with east–west contractional deformation phase documented along this sector of the DSFZ.
- In the Carmel Fault Zone, calcite precipitated directly onto the fault plane under open-space and fluid-filled conditions. The coating shows no subsequent deformation by repeated slip along the fault. Stable isotope composition suggests precipitation by karst processes, which involved CO_2-rich fluids migrating downwards

in the fault zone. Calcite fault-gouge precipitates in the Carmel Fault Zone are a mixture of host-rock gouge and authigenic calcite, and their overall geochemistry suggests pervasive fluid–rock interaction in the fault zone.

- In the Baraq Fault Zone, calcite precipitated within syntectonic tension gashes and veins. This occurred over a long period of time and during a pervasive fluid infiltration in the fault zone. The U–Th ages provide an average age of $417 \pm 30/25$ ka, with a maximum age of 540 ka. This age is in agreement with the youngest known activity along this fault zone.

We wish to thank Dr Y. Feng for providing technical assistance with U–Th TIMS analyses. Dr W.-P. (Sunny) Hu is thanked for her assistance with ICP-MS analyses. Ms K. Baublys is thanked for her kind help with stable isotope mass spectrometry and D. Thiede is thanked for his help with cathodoluminescence (CL) microscopy. The manuscript benefited from constructive reviews by S. Barker and an anonymous reviewer.

References

Akyuz, H. S., Altunel, E., Karabacak, V. & Yalciner, C. C. 2006. Historical earthquake activity of the northern part of the Dead Sea Fault Zone, southern Turkey. *Tectonophysics*, **426**, 281–293.

Amit, R., Zilberman, E., Porat, N. & Enzel, Y. 1999. Relief inversion in the Avrona Playa as evidence of large-magnitude historical earthquakes, Southern Arava Valley, Dead Sea Rift. *Quaternary Research*, **52**, 76–91.

Avni, Y. 1997. *Geological Evolution of the Central and Southern Negev as an Indicator of the Evolution of the Dead Sea Transform Western Margin in the Late Neogene and Quaternary*. PhD, Hebrew University.

Avni, Y., Bartov, Y., Garfunkel, Z. & Ginat, H. 2000. Evolution of the Paran drainage basin and its relation to the Plio-Pleistocene history of the Arava Rift western margin, Israel. *Israel Journal of Earth Sciences*, **49**, 215–238.

Avni, Y., Bartov, Y., Garfunkel, Z. & Ginat, H. 2001. The Arava Formation-A Pliocene sequence in the Arava Valley and its western margin, southern Israel. *Israel Journal of Earth Sciences*, **50**, 101–120.

Bar-Matthews, M., Ayalon, A., Gilmour, M., Matthews, A. & Hawkesworth, C. J. 2003. Sea–land oxygen isotopic relationships from planktonic foraminifera and speleothems in the Eastern Mediterranean region and their implication for paleorainfall during interglacial intervals. *Geochimica et Cosmochimica Acta*, **67**, 3181–3199.

Bar-Matthews, M., Ayalon, A. & Kaufman, A. 1997. Late Quaternary paleoclimate in the eastern mediterranean region from stable isotope analysis of speleothems at Soreq Cave, Israel. *Quaternary Research*, **47**, 155–168.

Barker, S. L. L., Cox, S. F., Eggins, S. M. & Gagan, M. K. 2006. Microchemical evidence for episodic growth of antitaxial veins during fracture-controlled fluid flow. *Earth and Planetary Science Letters*, **250**, 331–344.

Bau, M. & Dulski, P. 1999. Comparing yttrium and rare earths in hydrothermal fluids from the Mid-Atlantic Ridge: implications for Y and REE behaviour during near-vent mixing and for the Y/Ho ratio of proterozoic seawater. *Chemical Geology*, **155**, 77–90.

Bau, M. & Moller, P. 1992. Rare-earth element fractionation in metamorphogenic hydrothermal calcite, magnesite and siderite. *Mineralogy and Petrology*, **45**, 231–246.

Begin, Z. B., Steinberg, D. M., Ichinose, G. A. & Marco, S. 2005. A 40,000 year unchanging seismic regime in the Dead Sea rift. *Geology*, **33**, 257–260.

Ben-Menahem, A. & Aboodi, E. 1981. Micro- and macroseismicity of the Dead Sea rift and off-coast eastern Mediterranean. *Tectonophysics*, **80**, 199–233.

Boles, J. R. & Grivetti, M. 2000. Calcite cementation along the Refugio/Carneros fault, Coastal California: a link between deformation, fluid movement and fluid–rock interaction at a basin margin. *Journal of Geochemical Exploration*, **69–70**, 313–316.

Bolhar, R., Kamber, B. S., Moorbath, S., Fedo, C. M. & Whitehouse, M. J. 2004. Characterisation of early Archaean chemical sediments by trace element signatures. *Earth and Planetary Science Letters*, **222**, 43–60.

Boullier, A.-M., Fujimoto, K. *et al.* 2004. Textural evidence for recent co-seismic circulation of fluids in the Nojima fault zone, Awaji island, Japan. *Tectonophysics*, **378**, 165–181.

Bozkurt, E. 2001. Neotectonics of Turkey – a synthesis. *Geodinamica Acta*, **14**, 3–30.

Cheng, H., Edwards, R. L., Hoff, J., Gallup, C. D., Richards, D. A. & Asmerom, Y. 2000. The half-lives of uranium-234 and thorium-230. *Chemical Geology*, **169**, 17–33.

Choi, H. S., Yun, S. T., Koh, Y. K., Mayer, B., Park, S. S. & Hutcheon, I. 2009. Geochemical behavior of rare earth elements during the evolution of CO_2-rich groundwater: a study from the Kangwon district, South Korea. *Chemical Geology*, **262**, 334–343.

De Paola, N., Holdsworth, R. E. & Collettini, C. 2008. The internal structure of dilational stepovers in regional transtension zones. *International Geology Review*, **50**, 291–304.

Eggins, S. M., Woodhead, J. D. *et al.* 1997. A simple method for the precise determination of $\geq$40 trace elements in geological samples by ICPMS using enriched isotope internal standardisation. *Chemical Geology*, **134**, 311–326.

Eyal, M., Eyal, Y., Bartov, Y. & Steinitz, G. 1981. The tectonic development of the western margin of the Gulf of Elat (Aqaba) rift. *Tectonophysics*, **80**, 39–66.

Eyal, Y., Kaufman, A. & Bar-Matthews, M. 1992. Use of 230Th/U ages of striated carnotites for dating fault displacements. *Geology*, **20**, 829–832.

Flotte, N., Plagnes, V., Sorel, D. & Benedicto, A. 2001. Attempt to date Pleistocene normal faults of the Corinth-Patras Rift (Greece) by U/Th method, and tectonic implications. *Geophysical Research Letters*, **28**, 3769–3772.

Folk, R. L. 1965. Some aspects of recrystallization in ancient limestones. *In*: Pray, L. C. & Murray, R. C.

(eds) *Dolomitization and Limestones Diagnesis*. SEPM, Special Publications, **13**, 14–48.

Ford, D. C., Lundberg, J., Palmer, A. N., Palmer, M. V., Dreybrodt, W. & Schwarcz, H. P. 1993. Uranium-series dating of the draining of an aquifer; the example of Wind Cave, Black Hills, South Dakota; with Suppl. Data 9302. *Geological Society of America Bulletin*, **105**, 241–250.

Garfunkel, Z. 1998. Constrains on the origin and history of the Eastern Mediterranean basin. *Tectonophysics*, **298**, 5–35.

Grant, L. B., Mueller, K. J., Gath, E. M., Cheng, H., Edwards, R. L., Munro, R. & Kennedy, G. L. 1999. Late Quaternary uplift and earthquake potential of the San Joaquin Hills, southern Los Angeles basin, California. *Geology*, **27**, 1031–1034.

Gratier, J. P., Favreau, P., Renard, F. & Pili, E. 2002. Fluid pressure evolution during the earthquake cycle controlled by fluid flow and pressure solution crack sealing. *Earth, Planets and Space*, **54**, 1139–1146.

Hempton, M. R. 1987. Constraints on Arabian plate motion and extensional history of the Red Sea. *Tectonics*, **6**, 687–705.

Herece, E. 2008. *Geological Map along East Anatolian Fault-İslahiye Segment*. General Directorate of Mineral Research and Exploration, Ankara, Turkey.

Hickman, S. H., Sibson, R. & Bruhn, R. 1995. Introduction to special section: mechanical involvement of fluids in faulting. *Journal of Geophysical Research*, **100**, 15 441–15 449.

Inoue, M., Nohara, M., Okai, T., Suzuki, A. & Kawahata, H. 2004. Concentrations of trace elements in carbonate reference materials Coral JCp-1 and Giant Clam JCt-1 by inductively coupled plasma-mass spectrometry. *Geostandards and Geoanalytical Research*, **28**, 411–416.

Janssen, C., Romer, R. L., Hoffmann-Rothe, A., Mingram, B., Dulski, P., Möller, P. & Al-Zubi, H. 2005. The role of fluids in faulting deformation: a case study from the Dead Sea Transform (Jordan). *International Journal of Earth Sciences*, **94**, 243–255.

Janssen, C., Romer, R. L., Plessen, B., Naumann, R., Hoffmann-Rothe, A. & Matar, A. 2007. Contrasting fluid regimes along the Dead Sea Transform. *Geofluids*, **7**, 275–291.

Joffe, S. & Garfunkel, Z. 1987. Plate kinematics of the circum Red Sea-a re-evaluation. *Tectonophysics*, **141**, 5–22.

Johannesson, K. H., Farnham, I. M., Guo, C. & Stetzenbach, K. J. 1999. Rare earth element fractionation and concentration variations along a groundwater flow path within a shallow, basin-fill aquifer, southern Nevada, USA. *Geochimica et Cosmochimica Acta*, **63**, 2697–2708.

Johannesson, K. H. & Hendry, M. J. 2000. Rare earth element geochemistry of groundwaters from a thick till and clay-rich aquitard sequence, Saskatchewan, Canada. *Geochimica et Cosmochimica Acta*, **64**, 1493–1509.

Karabacak, V, Akyüz, S, Kiyak, N. G., Altunel, E, Meghraoui, M & Yönlü, Ö 2010. *Late Quaternary activity of the East Anatolian Fault Zone between Gölbaşı (Adıyaman) and Karataş (Adana)*. TÜBİTAK (The Scientific and Technological Research Council of Turkey) Project (109Y043), First Annual Report.

Kendall, A. C., Gonzalez, L. A., Carpenter, S. J. & Lohmann, K. C. 1993. Columnar calcite in speleothems; discussion and reply. *Journal of Sedimentary Petrology*, **63**, 550–552.

Klinger, Y., Avouac, J. P., Dorbath, L., Karaki, N. A. & Tisnerat, N. 2000. Seismic behaviour of the Dead Sea fault along Araba valley, Jordan. *Geophysical Journal International*, **142**, 769–782.

Ku, T.-L. 1965. An evaluation of the U^{234}/U^{238} method as a tool for dating pelagic sediments. *Journal of Geophysical Research*, **70**, 3457–3474.

Labaume, P., Carrio-Schaffhauser, E., Gamond, J.-F. & Renard, F. 2004. Deformation mechanisms and fluid-driven mass transfers in the recent fault zones of the Corinth Rift (Greece). *Comptes Rendus Geosciences*, **336**, 375–383.

Lawrence, M. G. & Kamber, B. S. 2006. The behaviour of the rare earth elements during estuarine mixing-revisited. *Marine Chemistry*, **100**, 147–161.

Lin, A. 1996. Injection veins of crushing-originated pseudotachylyte and fault gouge formed during seismic faulting. *Engineering Geology*, **43**, 213–224.

Liu, Y. G., Miah, M. R. U. & Schmitt, R. A. 1988. Cerium: a chemical tracer for paleo-oceanic redox conditions. *Geochimica et Cosmochimica Acta*, **52**, 1361–1371.

Ludwig, K. R. 1991. *ISOPLOT: A Plotting and Regression Program for Radiogenic-isotope Data; version 2.2*. US Geological Survey, Reston, VA.

Marco, S., Rockwell, T. K., Heimann, A., Frieslander, U. & Agnon, A. 2005. Late Holocene activity of the Dead Sea Transform revealed in 3D palaeoseismic trenches on the Jordan Gorge segment. *Earth and Planetary Science Letters*, **234**, 189–205.

Mart, Y., Ryan, W. B. F. & Lunina, O. V. 2005. Review of the tectonics of the Levant Rift system: the structural significance of oblique continental breakup. *Tectonophysics*, **395**, 209–232.

Matsuda, T., Omura, K. *et al.* 2004. Fracture-zone conditions on a recently active fault: insights from mineralogical and geochemical analyses of the Hirabayashi NIED drill core on the Nojima fault, southwest Japan, which ruptured in the 1995 Kobe earthquake. *Tectonophysics*, **378**, 143–163.

Miller, S. A., Collettini, C., Chiaraluce, L., Cocco, M., Barchi, M. & Kaus, B. J. P. 2004. Aftershocks driven by a high-pressure CO_2 source at depth. *Nature*, **427**, 724–727.

Muller, W. 2003. Strengthening the link between geochronology, textures and petrology. *Earth and Planetary Science Letters*, **206**, 237–251.

Nemer, T. & Meghraoui, M. 2006. Evidence of coseismic ruptures along the Roum fault (Lebanon): a possible source for the AD 1837 earthquake. *Journal of Structural Geology*, **28**, 1483–1495.

O'Neil, J. R., Clayton, R. N. & Mayeda, T. K. 1969. Oxygen isotope fractionation in divalent metal carbonates. *Journal of Chemical Physics*, **51**, 5547–5558.

Pili, É., Poitrasson, F. & Gratier, J.-P. 2002. Carbon–oxygen isotope and trace element constraints on how fluids percolate faulted limestones from the San

Andreas Fault system: partitioning of fluid sources and pathways. *Chemical Geology*, **190**, 231–250.

Plummer, L. N., Busenberg, E. & Riggs, A. C. 2000. In-situ growth of calcite at Devils Hole, Nevada: comparison of field and laboratory rates to a 500,000 year record of near-equilibrium calcite growth. *Aquatic Geochemistry*, **6**, 257–274.

Ramsay, J. G. 1980. The crack-seal mechanism of rock deformation. *Nature*, **284**, 135–139.

Reilinger, R. E., McClusky, S. C. *et al.* 1997. Global positioning system measurements of present-day crustal movements in the Arabia–Africa–Eurasia plate collision zone. *Journal of Geophysical Research*, **102**, 9983–9999.

Rotstein, Y., Shaliv, G. & Rybakov, M. 2004. Active tectonics of the Yizre'el valley, Israel, using high-resolution seismic reflection data. *Tectonophysics*, **382**, 31–50.

Schattner, U., Ben-Avraham, Z., Reshef, M., Bar-Am, G. & Lazar, M. 2006. Oligocene–Miocene formation of the Haifa basin: Qishon–Sirhan rifting coeval with the Red Sea-Suez rift system. *Tectonophysics*, **419**, 1–12.

Secor, D. T. 1965. Role of fluid pressure in jointing. *American Journal of Science*, **263**, 633–646.

Shapira, A. & Lea, F. 1987. Microseismicity of three locations along the Jordan Rift. *In*: Ben-Avraham, Z. (ed.) *Sedimentary Basins within the Dead Sea and Other Rift Zones. Tectonophysics*, **141,** 89–94.

Sibson, R. H. 1987. Earthquake rupturing as a mineralizing agent in hydrothermal systems. *Geology*, **15**, 701–704.

Skobelev, S. F., Hanon, M., Klerkx, J., Govorova, N. N., Lukina, N. V. & Kazmin, V. G. 2004. Active faults in Africa: a review. *Tectonophysics*, **380**, 131–137.

Sneh, A. & Weinberger, R. 2003. Geology of the Metulla quadrangle, northern Israel: implications for the offset along the Dead Sea Rift. *Israel Journal of Earth Sciences*, **52**, 123–138.

Steinitz, G. & Bartov, Y. 1991. The Miocene–Pleistocene history of the Dead Sea segment of the Rift in the light of K–Ar of basalts. *Israel Journal of Earth Sciences*, **40**, 199–208.

Sun, S.-S. & McDonough, W. F. 1989. Chemical and isotopic systematics of oceanic basalts: implications for mantle compositions and processes. *In*: Saunders, A. D. & Norry, M. J. (eds) *Magmatism in the Ocean Basins*. The Geological Society, London, Special Publications, **42**, 313–345.

Swart, P. K., Burns, S. J. & Leder, J. J. 1991. Fractionation of the stable isotopes of oxygen and carbon in carbon dioxide during the reaction of calcite with phosphoric acid as a function of temperature and technique. *Chemical Geology*, **86**, 89–96.

Szabo, B. J. & Rosholt, J. N. 1989. Uranium-series nuclides in the Golden fault, Colorado, U.S.A.: dating latest fault displacement and measuring recent uptake of radionuclides by fault-zone materials. *Applied Geochemistry*, **4**, 177–182.

Taymaz, T., Westaway, R. & Reilinger, R. 2004. Active faulting and crustal deformation in the Eastern Mediterranean region. *Tectonophysics*, **391**, 1–9.

Uysal, I. T., Mutlu, H., Altunel, E., Karabacak, V. & Golding, S. D. 2006. Clay mineralogical and isotopic (K–Ar, $\delta^{18}O$, δD) constraints on the evolution of the North Anatolian Fault Zone, Turkey. *Earth and Planetary Science Letters*, **243**, 181–194.

Uysal, I. T., Feng, Y. *et al.* 2007. U-series dating and geochemical tracing of late Quaternary travertine in co-seismic fissures. *Earth and Planetary Science Letters*, **257**, 450–462.

Uysal, I. T., Feng, Y.-X., Zhao, J.-X., Isik, V., Nuriel, P. & Golding, S. D. 2009. Hydrothermal CO_2 degassing in seismically active zones during the late Quaternary. *Chemical Geology*, **265**, 442–454.

Uysal, I. T., Feng, Y.-X. *et al.* 2011. Seismic cycles recorded in late Quaternary calcite veins: geochronological, geochemical and microstructural evidence. *Earth and Planetary Science Letter*, **303**, 84–96.

Vaks, A., Bar-Matthews, M. *et al.* 2003. Paleoclimate reconstruction based on the timing of speleothem growth and oxygen and carbon isotope composition in a cave located in the rain shadow in Israel. *Quaternary Research*, **59**, 182–193.

Vaks, A., Bar-Matthews, M., Matthews, A., Ayalon, A. & Frumkin, A. 2010. Middle–Late Quaternary paleoclimate of northern margins of the Saharan–Arabian Desert: reconstruction from speleothems of Negev Desert, Israel. *Quaternary Science Reviews*, **29**, 2647–2662.

Van der Pluijm, B. A., Hall, C. M., Vroliik, P. J. & Pevear, D. R. 2001. The dating of shallow faults in the Earth's crust. *Nature*, **412**, 172–175.

van Eck, T. & Hofstetter, A. 1990. Fault geometry and spatial clustering of microearthquakes along the Dead Sea–Jordan rift fault zone. *In*: Kovach, R. L. & Ben-Avraham, Z. (eds) *Geologic and Tectonic Processes of the Dead Sea Rift Zone. Tectonophysics*, **180**, 15–27.

Verhaert, G., Muchez, P. *et al.* 2004. Origin of palaeofluids in a normal fault setting in the Aegean region. *Geofluids*, **4**, 300–314.

Verhaert, G., Muchez, P., Sintubin, M., Similox-Tohon, D., Vandycke, S. & Waelkens, M. 2003. Reconstruction of neotectonic activity using carbonate precipitates: a case study from the northwestern extremity of the Isparta Angle (SW Turkey). *Journal of Geochemical Exploration*, **78–79**, 197–201.

Vroljik, P. J. & Van der Pluijm, B. A. 1999. Clay gouge. *Journal of Structural Geology*, **21**, 1039–1048.

Weinberger, R., Gross, M. R. & Sneh, A. 2009. Evolving deformation along a transform plate boundary: example from the Dead Sea Fault in northern Israel. *Tectonics*, **28**, doi:10.1029/2008TC002316.

Westaway, R. 1994. Present day kinematics of the Middle East and Eastearn Mediterranean sea. *Journal of Geophysical Research*, **99**, 12 072–12 096.

Westaway, R. & Arger, J. 1996. The Golbasi basin, southeastern Turkey: a complex discontinuity in a major strike–slip fault zone. *Journal of the Geological Society, London*, **153**, 729–744.

Wood, S. A. 1990. The aqueous geochemistry of the rare-earth elements and yttrium. 1. Review of available low-temperature data for inorganic complexes and the

inorganic REE speciation of natural-waters. *Chemical Geology*, **82**, 159–186.

YAN, Y., VAN DER PLUIJM, B. A. & PEACOR, D. R. 2001. Deformation microfabrics of clay gouge, Lewis Thrust, Canada: a case for Fault weakening from clay transformation. *In*: HOLDSWORTH, R. E., STRACHAN, R. A., MAGLOUGHLIN, J. F. & KNIPE, R. J. (eds) *The Nature and Tectonic Significance of Fault Zone Weakening*. Geological Society, London, Special Publications, **186**, 103–112.

YU, K.-F., ZHAO, J.-X., SHI, Q., CHEN, T.-G., WANG, P.-X., COLLERSON, K. D. & LIU, T.-S. 2006. U-series dating of dead Porites corals in the South China sea: evidence for episodic coral mortality over the past two centuries. *Quaternary Geochronology*, **1**, 129–141.

ZHAO, J.-X, HU, K., COLLERSON, K. D. & XU, H. 2001. Thermal ionization mass spectrometry U-series dating of a hominid site near Nanjing, China. *Geology*, **29**, 27–30.

ZILBERMAN, E., AMIT, R., PORAT, N., ENZEL, Y. & AVNER, U. 2005. Surface ruptures induced by the devastating 1068 AD earthquake in the southern Arava valley, Dead Sea Rift, Israel. *Tectonophysics*, **408**, 79–99.